Journal of Non-Newtonian Fluid Mechanics 214 (2014) 28–37

Contents lists available at ScienceDirect

Journal of Non-Newtonian Fluid Mechanics

journal homepage: http://www.elsevier.com/locate/jnnfm

Slip flows of Newtonian and viscoelastic fluids in a 4:1 contraction

L.L. Ferrás [a,*], A.M. Afonso [b], M.A. Alves [b], J.M. Nóbrega [a], O.S. Carneiro [a], F.T. Pinho [c]

[a] Institute for Polymers and Composites/I3N, University of Minho, Campus de Azurém, 4800-058 Guimarães, Portugal
[b] Departamento de Engenharia Química, CEFT, Faculdade de Engenharia da Universidade do Porto, Rua Dr. Roberto Frias s/n, 4200-465 Porto, Portugal
[c] Centro de Estudos de Fenómenos de Transporte, Faculdade de Engenharia da Universidade do Porto, Rua Dr. Roberto Frias s/n, 4200-465 Porto, Portugal

ARTICLE INFO

Article history:
Received 1 August 2012
Received in revised form 10 September 2014
Accepted 15 September 2014
Available online 23 September 2014

Keywords:
4:1 contraction
Slip boundary condition
sPTT model
Finite volume method

ABSTRACT

This work presents a numerical study of the 4:1 planar contraction flow of a viscoelastic fluid described by the simplified Phan-Thien–Tanner model under the influence of slip boundary conditions at the channel walls. The linear Navier slip law was considered with the dimensionless slip coefficient varying in the range $[0; 4500]$. The simulations were carried out for a small constant Reynolds number of 0.04 and Deborah numbers (De) varying between 0 and 5. Convergence could not be achieved for higher values of the Deborah number, especially for large values of the slip coefficient, due to the large stress gradients near the singularity of the reentrant corner.

Increasing the slip coefficient leads to the formation of two vortices, a corner and a lip vortex. The lip vortex grows with increasing slip until it absorbs the corner vortex, creating a single large vortex that continues to increase in size and intensity. In the range $De = 3–5$ no lip vortex was formed. The flow is characterized in detail for $De = 1$ as function of the slip coefficient, while for the remaining De only the main features are shown for specific values of the slip coefficient.

1. Introduction

In industrial processes, such as those involved in polymer processing, the existence of contraction flows is very common. The development of vortices in these geometries affects the smoothness of the flow and promotes the appearance of instabilities, as reported by Kim and Dealy [1] and Miller et al. [2]. The flow through a 4:1 planar sudden contraction under conditions of creeping flow and no wall slip is a long standing classic benchmark problem in computational rheology [3].

A wide range of experimental, theoretical and numerical studies have been carried out in the past regarding contraction flows of Newtonian and non-Newtonian fluids. For the experimental work we highlight the book of Boger and Walters [4] where most of the relevant non-Newtonian flow phenomena are illustrated. Other interesting flow dynamics features, related to elasticity, were also reported experimentally, as the divergent streamlines [5], characterized by a strong curvature of the upstream streamlines moving away from the centerline towards the duct walls; the *cat's ears* phenomenon found in smooth contraction flows [6,7], where the nearly 2D flow suddenly exhibits strong velocity overshoots near the walls at the contraction region; and the secondary flow inversion observed in 3D square/square contractions [8,9], in which the flow direction inside the separated flow region is reversed due to viscoelasticity. Extensive literature reviews of experiments in contraction flow were presented by McKinley et al. [10] and Owens and Phillips [3], where they show that, for some shear-thinning fluids, there is corner vortex enhancement following the formation of a lip vortex, which initially grows and subsequently merges with the corner vortex, whereas for Boger fluids the lip vortex mechanism is absent and the corner vortex keeps growing with De. For all fluids the steady single corner vortex keeps growing with De until the flow eventually becomes unsteady above a critical De. In terms of theoretical investigations of viscoelastic flow in the vicinity of the reentrant corner in a planar contraction we highlight the works by Hinch [11], Renardy [12] and a series of investigations by Evans and Sibley [13,14]. In terms of numerical simulation the monograph by Owens and Phillips [3] gives a detailed overview of the progress in numerical analysis, and an in depth review on the pioneering numerical works can be found in Keunings [15]. There are several other important works on contraction flows, such as Refs. [5,9,16–22].

All these works assume the usually employed no-slip boundary condition at the walls. The few exceptions that we are aware of regarding contraction flows with wall slip, are the numerical works of Sunarso et al. [23,24] investigating the effect of wall slip on the

* Corresponding author.
E-mail addresses: luis.ferras@dep.uminho.pt (L.L. Ferrás), aafonso@fe.up.pt (A.M. Afonso), mmmalves@fe.up.pt (M.A. Alves), mnobrega@dep.uminho.pt (J.M. Nóbrega), olgasc@dep.uminho.pt (O.S. Carneiro), fpinho@fe.up.pt (F.T. Pinho).

http://dx.doi.org/10.1016/j.jnnfm.2014.09.007
0377-0257/

flow behavior in macro and micro contraction channels, Yasuda and Sugiura's [25] experimental and numerical studies of contraction flows with the nonlinear Navier slip boundary condition, and the analytical study of inertialess planar contraction flow of Joshi and Denn [26] with the linear Navier slip boundary condition. Although Sunarso et al. [23,24] have analyzed this problem, they used a different constitutive equation (single mode FENE-P model) and their investigation is limited to a small range of slip coefficients.

The challenge of establishing quantitative agreement between the numerical results and the experimental observations is a demanding need [27] and this cannot be achieved if the correct boundary conditions are not applied. It is known that various polymer melts exhibit wall slip [28–30] but when modeling viscoelastic flows, wall slip velocity is usually not taken into account. It is therefore important to assess the influence of wall slip velocity on the fluid flow and, for that reason, this work presents a numerical study of the 4:1 contraction flow with the Navier slip boundary condition for a large range of dimensionless slip coefficients, $k_l^* \in [0;4500]$, and Deborah numbers, $De \in \{0;1;2;3;4;5\}$. This geometry was chosen in order to investigate the direct influence of the slip velocity by analyzing the vortex sizes. Both Newtonian and non-Newtonian fluids modeled by the simplified PTT model (sPTT) are studied. A detailed study of the flow characteristics, focusing on the influence of wall slip velocity coefficient on the vortex growth, intensity and sizes is provided. For such purpose, we use an efficient procedure that calculates the slip velocity along the iterations of the numerical procedure, by incrementally increasing the slip velocity, so that a smaller slip velocity than the velocity at the center of the nearest computational cell, is obtained (a necessary condition to avoid numerical divergence [31]).

This introduction is followed by Section 2 where the governing equations together with the wall slip boundary condition employed are presented. In Section 3 we briefly describe the algorithm used to solve the governing equations and we present the geometry and the flow characteristics. The results are presented and discussed in Section 4, divided into three parts: first, the slip flow is analyzed for Newtonian fluids, followed by a detailed investigation of the flow of the sPTT fluid for $De = 1$ and finally the main flow features for the remaining studied Deborah numbers. The main conclusions close the paper.

2. Governing equations

The governing equations for confined flow of incompressible fluids are the continuity,

$$\nabla \cdot \mathbf{u} = 0 \tag{1}$$

and the momentum,

$$\rho \frac{\partial \mathbf{u}}{\partial t} + \rho \nabla \cdot (\mathbf{u}\mathbf{u}) = -\nabla p + \nabla \cdot \boldsymbol{\tau} \tag{2}$$

equations, where $\mathbf{u}$ is the velocity vector, p is the pressure, ρ is the fluid density and $\boldsymbol{\tau} = \boldsymbol{\tau}_s + \boldsymbol{\tau}_p$ is the deviatoric stress tensor. The stress tensor is given as a sum of a solvent contribution, $\boldsymbol{\tau}_s = \eta_s\left(\nabla\mathbf{u} + (\nabla\mathbf{u})^T\right)$ (where η_s is the solvent viscosity) and a polymer contribution, $\boldsymbol{\tau}_p$, which in this case is described by the simplified Phan-Thien–Tanner (sPTT) model [32]:

$$f(\mathrm{tr}\,\boldsymbol{\tau}_p)\boldsymbol{\tau}_p + \lambda\left(\frac{\partial \boldsymbol{\tau}_p}{\partial t} + \mathbf{u}\cdot\nabla\boldsymbol{\tau}_p - \left[(\nabla\mathbf{u})^T\cdot\boldsymbol{\tau}_p + \boldsymbol{\tau}_p\cdot\nabla\mathbf{u}\right]\right) = \eta_p\left(\nabla\mathbf{u} + (\nabla\mathbf{u})^T\right) \tag{3}$$

where $f(\mathrm{tr}\,\boldsymbol{\tau})$ is a function depending on the trace of the stress tensor, λ is the polymer relaxation time and η_p is the polymer viscosity coefficient. For the function $f(\mathrm{tr}\boldsymbol{\tau})$ we use its linear form, given by

$$f(\mathrm{tr}\,\boldsymbol{\tau}_p) = 1 + \frac{\varepsilon\lambda}{\eta_p}\mathrm{tr}(\boldsymbol{\tau}_p) \tag{4}$$

where ε is the extensibility parameter that bounds the steady-state extensional viscosity of the sPTT fluid. This constitutive equation was chosen because it has been extensively studied in contraction flows in the absence of slip (see Alves et al. [20] and the literature cited therein).

In order to include the wall slip boundary condition, the usual no-slip boundary condition ($\mathbf{u} = \mathbf{0}$) was replaced by the Navier slip law [33] at the wall,

$$\mathbf{u}_{wall} = -k_l\{\mathbf{n}\cdot\boldsymbol{\tau} - [(\mathbf{n}\cdot\boldsymbol{\tau})\cdot\mathbf{n}]\mathbf{n}\} \tag{5}$$

where $\mathbf{n}$ is the unit normal vector at the boundary, and $k_l \in [0,+\infty)$ is the slip coefficient that controls the intensity of wall slip velocity. Eq. (5) states that the wall velocity $\mathbf{u}_{wall}$ (tangent to the wall) is in the opposite direction to the surface traction force $\mathbf{n}\cdot\boldsymbol{\tau}$.

3. Numerical method and geometry

The system of Eqs. (1)–(3) is solved using a methodology based on the finite volume method algorithm. The SIMPLEC method of Van Doormaal and Raithby [34], extended by Oliveira et al. [35] to incorporate viscoelastic fluids, is used to couple velocity, pressure and stress fields [35]. The efficient handling of slip boundary conditions requires some changes in the overall procedure that are now described. For simplicity and ease of understanding we assume a 2D flow and the existence of slip velocity at a north wall face (see Fig. 1).

The discretization of the continuity equation, Eq. (1), results in the flux balance for each computational cell (see [35] for more details). Because there is no fluid crossing the impermeable wall ($\mathbf{u}\cdot\mathbf{n} = 0$), the assumption of slip velocity does not alter the usual discretization (considering the no-slip boundary condition) of this equation. In the discretization of the momentum equation, Eq. (2), the only term that is affected by the slip velocity is the diffusive term and the boundary at the wall, that comprises the contribution from both the solvent and the polymer.

The integration of the 2D momentum equation, specifically the second term on the right-hand-side of Eq. (2) leads to the following expressions, for x and y momentum equations, respectively,

$$\int_V \nabla\cdot\left[\tau_{xx_p},\tau_{xy_p}\right]dV + \int_V \nabla\cdot\left[\eta_s\left(2\frac{\partial u}{\partial x},\frac{\partial u}{\partial y}+\frac{\partial v}{\partial x}\right)\right]dV \tag{6}$$

$$\int_V \nabla\cdot\left[\tau_{xy_p},\tau_{yy_p}\right]dV + \int_V \nabla\cdot\left[\eta_s\left(\frac{\partial v}{\partial x}+\frac{\partial u}{\partial y},2\frac{\partial v}{\partial y}\right)\right]dV \tag{7}$$

The use of the Gauss theorem results in the following discretization,

$$\left(\tau_{xy_p}+\eta_s\left(\frac{\partial u}{\partial y}+\frac{\partial v}{\partial x}\right)\right)_{wall}A_{wall} - \left(\tau_{xy_p}+\eta_s\left(\frac{\partial u}{\partial y}+\frac{\partial v}{\partial x}\right)\right)_{s}A_s + \left(\tau_{xx_p}+2\eta_s\frac{\partial u}{\partial x}\right)_{e}A_e - \left(\tau_{xx_p}+2\eta_s\frac{\partial u}{\partial x}\right)_{w}A_w \tag{8}$$

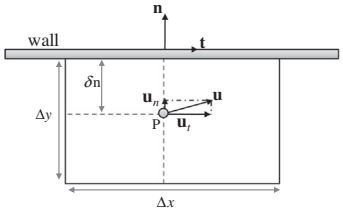

Fig. 1. Computational cell near the wall.

$$\left(\tau_{yy_p}+2\eta_s\frac{\partial v}{\partial y}\right)_{wall}A_{wall}-\left(\tau_{yy_p}+2\eta_s\frac{\partial v}{\partial y}\right)_s A_s + \left(\tau_{xy_p}+\eta_s\left(\frac{\partial v}{\partial x}+\frac{\partial u}{\partial y}\right)\right)_e A_e-\left(\tau_{xy_p}+\eta_s\left(\frac{\partial v}{\partial x}+\frac{\partial u}{\partial y}\right)\right)_w A_w \quad (9)$$

where A stands for the area of the control volume face. For the evaluation of τ_{xy} and τ_{yy} at the wall, linear extrapolation was chosen. Note that because we use a non-staggered collocated grid, the stresses are calculated at the center of the control volumes.

For the evaluation of $\eta_s\frac{\partial u}{\partial y}$ and $\eta_s\frac{\partial v}{\partial y}$ at the wall, we can use, for example, a one-sided first-order finite difference,

$$\left(\frac{\partial\phi}{\partial y}\right)_{wall}=\frac{\phi_{wall}-\phi_P}{\Delta y_f}+O(\Delta y), \quad (10)$$

where $\phi=u$ for the x-momentum equation and $\phi=v$ for the y-momentum equation, and Δy_f represents the cell half-width in the wall normal direction. For the particular case of the cell used to illustrate the calculation process (see Fig. 1) for the x-momentum equation the variable u_{wall} corresponds to the slip velocity that results from the slip model, while $v_{wall}=0$ and consequently $\left(\frac{\partial v}{\partial x}\right)_{wall}=0$.

The solution of the constitutive equation is also affected by the slip velocity. Consider Eq. (3) written in Cartesian coordinates (for simplicity the subscript p is dropped in the Cartesian components of the polymer extra stress),

$$\begin{cases} f(\mathrm{tr}\,\boldsymbol{\tau}_p)\tau_{xx}+\lambda\left(\frac{\partial\tau_{xx}}{\partial t}+u\frac{\partial\tau_{xx}}{\partial x}+v\frac{\partial\tau_{xx}}{\partial y}\right)=2\eta_p\frac{\partial u}{\partial x}+2\lambda\left(\tau_{xx}\frac{\partial u}{\partial x}+\tau_{xy}\frac{\partial u}{\partial y}\right)\\ f(\mathrm{tr}\,\boldsymbol{\tau}_p)\tau_{xy}+\lambda\left(\frac{\partial\tau_{xy}}{\partial t}+u\frac{\partial\tau_{xy}}{\partial x}+v\frac{\partial\tau_{xy}}{\partial y}\right)=\eta_p\left(\frac{\partial u}{\partial y}+\frac{\partial v}{\partial x}\right)\\ \quad+\lambda\left(\tau_{xx}\frac{\partial v}{\partial x}+\tau_{yy}\frac{\partial u}{\partial y}+\tau_{xy}\left(\frac{\partial u}{\partial x}+\frac{\partial v}{\partial y}\right)\right)\\ f(\mathrm{tr}\,\boldsymbol{\tau}_p)\tau_{yy}+\lambda\left(\frac{\partial\tau_{yy}}{\partial t}+u\frac{\partial\tau_{yy}}{\partial x}+v\frac{\partial\tau_{yy}}{\partial y}\right)=2\eta_p\frac{\partial v}{\partial y}+2\lambda\left(\tau_{xy}\frac{\partial v}{\partial x}+\tau_{yy}\frac{\partial v}{\partial y}\right)\end{cases} \quad (11)$$

At the computational control volume bordering the wall, the left-hand-side of this system of equations is not influenced by the slip velocity, as shown in the discretization given below (for a general stress component τ_{ij})

$$(\Delta Vf(\mathrm{tr}\,\boldsymbol{\tau}_p))_P\tau_{ij_P}+\lambda\frac{\Delta V\left(\tau_{ij_P}-\tau^0_{ij_P}\right)}{\Delta t}+\lambda\left(F_e\tau_{ij_e}-F_w\tau_{ij_w}+F_n\tau_{ij_n}-F_s\tau_{ij_s}\right) \quad (12)$$

where F_f is the flow rate that crosses face f (with f equal to e, w, n and s). For the cell under consideration F_n is null. In the discretization of the transient term, we consider a first-order Euler method. We note that the first-order of this integration has no influence in the accuracy of the steady-state results reported in this work.

The discretization of the right-hand-side of Eq. (11) in a cell with a north wall face is given by,

$$\begin{cases} 2\eta_p\frac{\Delta V}{\delta x}(u_e-u_w)+2\lambda\Delta V\left(\tau_{xx_P}\frac{u_e-u_w}{\delta x}+\tau_{xy_P}\frac{u_{wall}-u_s}{\delta y}\right)\\ \eta_p\frac{\Delta V}{\delta y}(u_{wall}-u_s)+\eta_p\frac{\Delta V}{\delta x}(v_e-v_w)+\lambda\Delta V\left(\tau_{xx_P}\frac{v_e-v_w}{\delta x}\right.\\ \quad\left.+\tau_{yy_P}\frac{u_{wall}-u_s}{\delta y}+\tau_{xy_P}\left(\frac{u_e-u_w}{\delta x}+\frac{v_{wall}-v_s}{\delta y}\right)\right)\\ 2\eta_p\frac{\Delta V}{\delta y}(v_{wall}-v_s)+2\lambda\Delta V\left(\tau_{xy_P}\frac{v_e-v_w}{\delta x}+\tau_{yy_P}\frac{v_{wall}-v_s}{\delta y}\right)\end{cases} \quad (13)$$

where u_{wall} is the slip velocity evaluated with the slip model and $v_{wall}=0$ (for a north wall). Note that for an east wall cell face we would have $u_{wall}=0$ and $v_{wall}\neq 0$.

In order to determine the slip velocity we need to use the slip model, here given by Eq. (5). For the particular geometry used in our simulations, which is a contraction, we only have walls at the north and east cell faces. For a north wall cell face we have that,

$$[u_{wall},v_{wall}]=-k_l\left[\tau_{xy_p}+\eta_s\frac{\partial u}{\partial y},0\right]_{wall}\approx-k_l\left[\tau_{xy_p}+\eta_s\frac{u_{wall}-u_P}{\Delta y_f},0\right]_{wall} \quad (14)$$

and for an east wall cell face we obtain,

$$[u_{wall},v_{wall}]=-k_l\left[0,\tau_{xy_p}+\eta_s\frac{\partial v}{\partial x}\right]_{wall}\approx-k_l\left[0,\tau_{xy_p}+\eta_s\frac{v_{wall}-v_P}{\Delta x_f}\right]_{wall} \quad (15)$$

where τ_{xy_p} is the polymeric shear stress at the wall, obtained by linear extrapolation of the shear stresses at the nearest cell centers in the normal direction.

To solve the system of equations the following iterative procedure is used:

(1) Set the boundary conditions, the initial (tentative) velocity, stress and pressure fields.
(2) Solve the extra-stress equations for the non-Newtonian model, Eqs. (12) and (13).
(3) Compute the wall-slip velocity with the discretized slip model, Eqs. (14) and (15).
(4) Solve the linearized momentum equations.
(5) Solve the pressure correction equation.
(6) Correct the velocity and pressure fields.
(7) Check for convergence of the residuals of the linear system of discretized equations.
(8) If convergence is not achieved return to step 2 at new time level and repeat until convergence.

Since we are looking for the steady state solution the use of a pseudo-time evolution is only for relaxation purposes, i.e., each time step represents one iteration i.

Since there is no control over the evolution and growth of the slip velocity, for most cases it is mandatory to use under-relaxation, $u^{i*}_{ws}=Ru^i_{ws}+(1-R)u^{i-1}_{ws}$, with $0<R<1$. The relaxation factor R can be a function of the difference between the slip velocity and the velocity at the center of the nearest computational cell, $|u_P-u_{ws}|$ (an essential condition for convergence is $u_{ws}<u_P$ [31]), resulting in the use of significant under-relaxation factor at the beginning of the iterative process, which can subsequently be reduced as the numerical solution converges. We also used as convergence criteria in step 7 (besides the usual convergence criteria based on the residuals of the momentum, pressure and constitutive equations), the residual, *Res*, resulting from the difference between the slip velocity evaluated by Eqs. (14) and (15) and the slip velocity obtained from the use of classical relaxation. This new residual is given by,

$$Res=\sum_j Res(j) \quad (16)$$

where j index spans over all wall cell faces (north and east faces for the present case study).

Note that in a previous work [31], we proposed a different method to calculate the slip velocity at the wall. That method is more stable, but at the cost of neglecting stress advection at the wall. The method described in [31] provided slight different results when compared to the more accurate method proposed in this work, when considering viscoelastic fluids.

3.1. Geometry

The geometry of the 4:1 contraction used in the present study is given in Fig. 2. The computational domain was divided into five blocks (see Table 1 and Fig. 2) and only half of the channel is considered because of symmetry. We use three different meshes (MC1, MC2 and MC3 – Table 1). Refinement between consecutive meshes is consistently done by doubling the number of cells in each

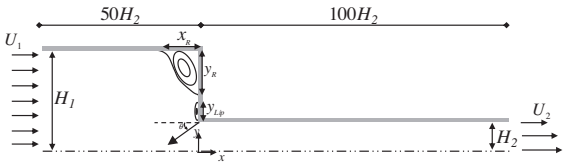

Fig. 2. Schematic representation of the 4:1 contraction geometry.

direction and using square-rooted cell contraction/expansion factors. The notation n_x and n_y is used to represent the number of cells in the x and y directions, respectively, f_x and f_y are the contraction/expansion ratios between sizes of consecutive cells that allow to adjust the concentration of cells in zones where high gradients are expected to occur. The most refined mesh (MC3) has 199,344 cells and a zoomed view of the more refined zone is shown in Fig. 3. More details regarding these three meshes can be found in Table 1. The simulations were performed for the sPTT model at a constant Reynolds number, $Re = \rho U_2 H_2/\eta_0 = 0.04$ and varying Deborah numbers, $De = \lambda U_2/H_2$ ($De = 0; 1; 2; 3; 4$ and 5) with $\varepsilon = 0.25$ and a viscosity ratio $\beta = \frac{\eta_s}{\eta_0} = \frac{\eta_s}{\eta_s+\eta_p} = \frac{1}{9}$.

4. Results and discussion

4.1. Newtonian fluids

4.1.1. Vortex size and intensity

For Newtonian fluids ($De = 0$) the increase of the slip coefficient leads to a significant variation of the vortex intensity Ψ_R and vortex sizes $X_R = x_R/H_2$ and $Y_R = y_R/H_2$ (cf. Fig. 2). The vortex intensity is defined as the flow rate per unit depth inside the vortex normalized by the flow rate per unit depth at the entrance, U_1H_1:

$$\Psi_R = \frac{\psi_R - U_1H_1}{U_1H_1} \times 10^3 \tag{17}$$

where ψ_R is the streamfunction value at the vortex center (we consider $\psi_R = 0$ at the centerline, $y = 0$). As shown in Figs. 4 and 5, the vortex decreases with the increase of the slip coefficient and it disappears at $k_l^* = \frac{k_l\eta_0}{H_2} \approx 50$. Regarding the vortex intensity, we found that it increases from $k_l^* = 0$ to $k_l^* \approx 0.5$ and then decreases until vanishing when k_l^* further increases. For a small amount of slip the flow is essentially affected only in the vicinity of the wall where there is a reduction of the shear rates with accompanying reductions in dissipative friction, thus increasing the vortex strength while the vortex remains essentially unchanged (cf. Fig. 4). As k_l^* is further increased the slip effect penetrates further into the channel and leads to a reduction in size and consequently in the strength of the recirculation. With a very large slip coefficient, the flow behaves essentially as an inviscid fluid flow, which is able to negotiate all the obstacles and no recirculation develops.

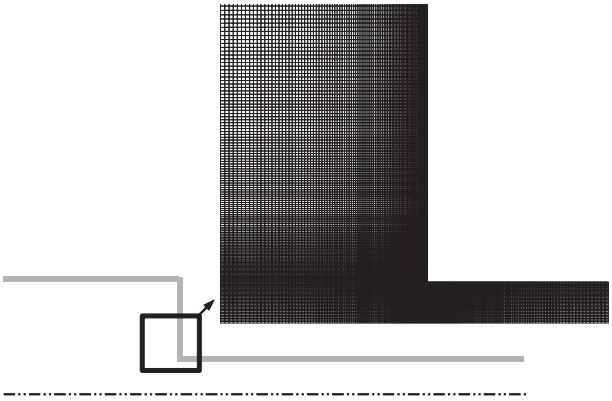

Fig. 3. Zoomed view of mesh MC3.

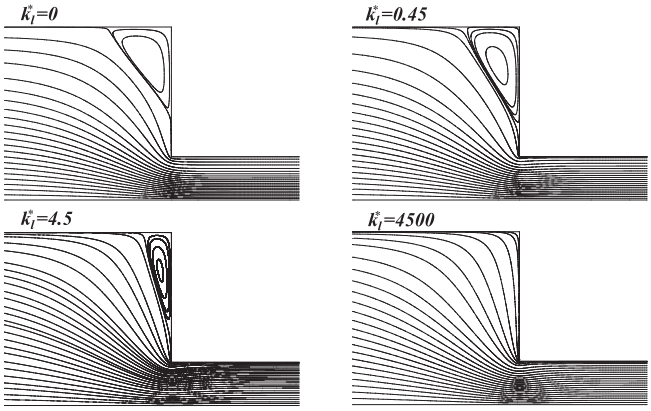

Fig. 4. Flow patterns as function of the dimensionless slip coefficient k_l^* for a Newtonian fluid at $Re = 0.04$.

4.1.2. Singularity behavior (variation along the line $\theta = \pi/2$)

In all Newtonian fluid flow cases there was no lip vortex and this allowed the measurement of the asymptotic variation of the stress and velocity components in the vicinity of the reentrant corner at $\theta = \pi/2$ measured counterclockwise from the incoming flow direction (cf. Fig. 2). This way we can compare our results with the theoretical studies of Moffatt [36], and Dean and Montagnon [37], for the asymptotic behavior of a fluid near the reentrant corner (Fig. 6). These authors found that the asymptotic behavior of velocity and stress components near the reentrant corner are given by [37],

$$u_i \propto r^{0.545}, \quad \tau_{ij} \propto r^{-0.455} \tag{18}$$

where r is the distance measured from the reentrant corner. In Fig. 6 we can see a good agreement between the no slip numerical results

Table 1
Mesh characteristics for MC1, MC2, MC3.

Zone	MCI				MC2				MC3			
	f_x	f_y	n_x	n_y	f_x	f_y	n_x	n_y	f_x	f_y	n_x	n_y
1	0.93500	0.95950	87	36	0.96695	0.97950	174	72	0.98334	0.98972	348	144
2	0.93500	1.04860	87	47	0.96695	1.02400	174	94	0.98334	1.01193	348	188
3	0.93500	0.92700	87	18	0.96695	0.96280	174	36	0.98334	0.98123	348	72
4	1.06952	0.95950	87	36	1.03418	0.97950	174	72	1.01694	0.98972	348	144
5	1.00000	0.95950	15	36	1.00000	0.97950	30	72	1.00000	0.98972	60	144
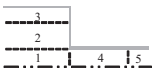		nº cells		12459		nº cells		49836		nº cells		199344
		(Δ/H)min		0.010		(Δ/H)min		0.005		(Δ/H)min		0.0025

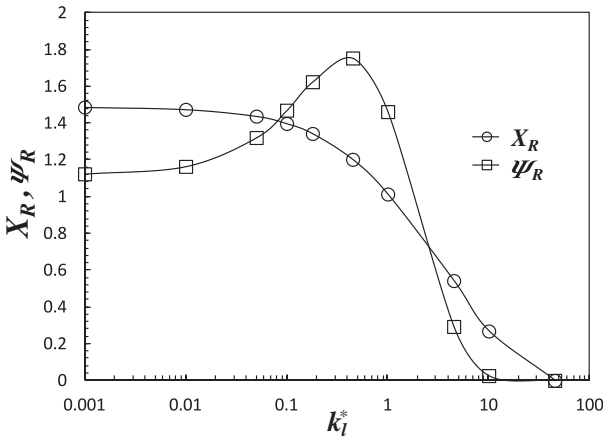

Fig. 5. Variation of the vortex dimension X_R and vortex intensity Ψ_R with the dimensionless slip coefficient k_l^* for $Re = 0.04$ and $De = 0$. Results computed with mesh MC3.

($k_l^* = 0$) and those predicted by Eq. (18) which allow us to confirm the accuracy of the numerical results.

4.1.3. Couette correction

In order to investigate the entry viscous losses, we also studied the variation of the Couette correction with the slip coefficient. The Couette correction is given by [38],

$$C = \frac{\Delta p - \Delta p_{1FD} - \Delta p_{2FD}}{2\tau_w} \tag{19}$$

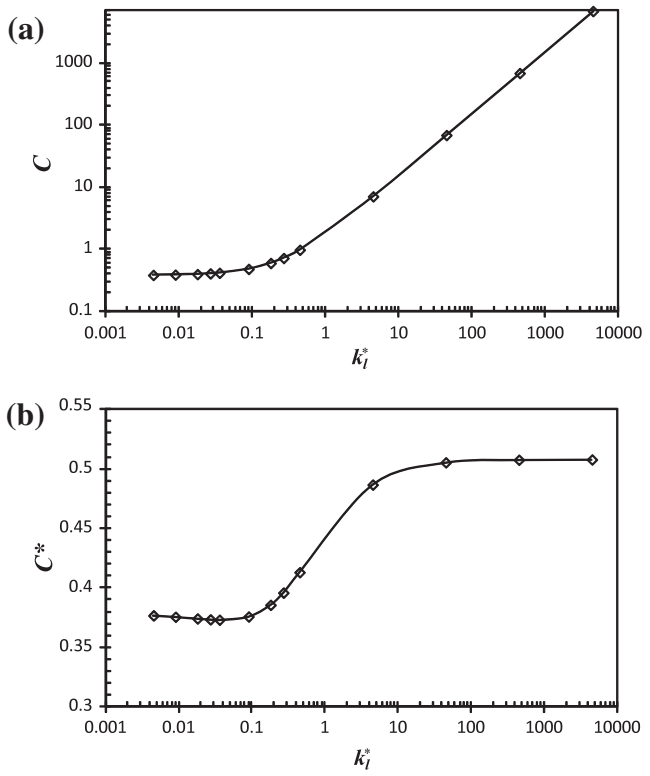

Fig. 7. Variation of the Couette correction with the dimensionless slip coefficient for a Newtonian fluid at $Re = 0.04$. (a) Couette correction (C) normalized with $2\tau_w$. (b) Couette correction (C^*) normalized with the wall shear stress from the no-slip case, $2\tau_{w-no\ slip}$. Results computed with mesh MC3.

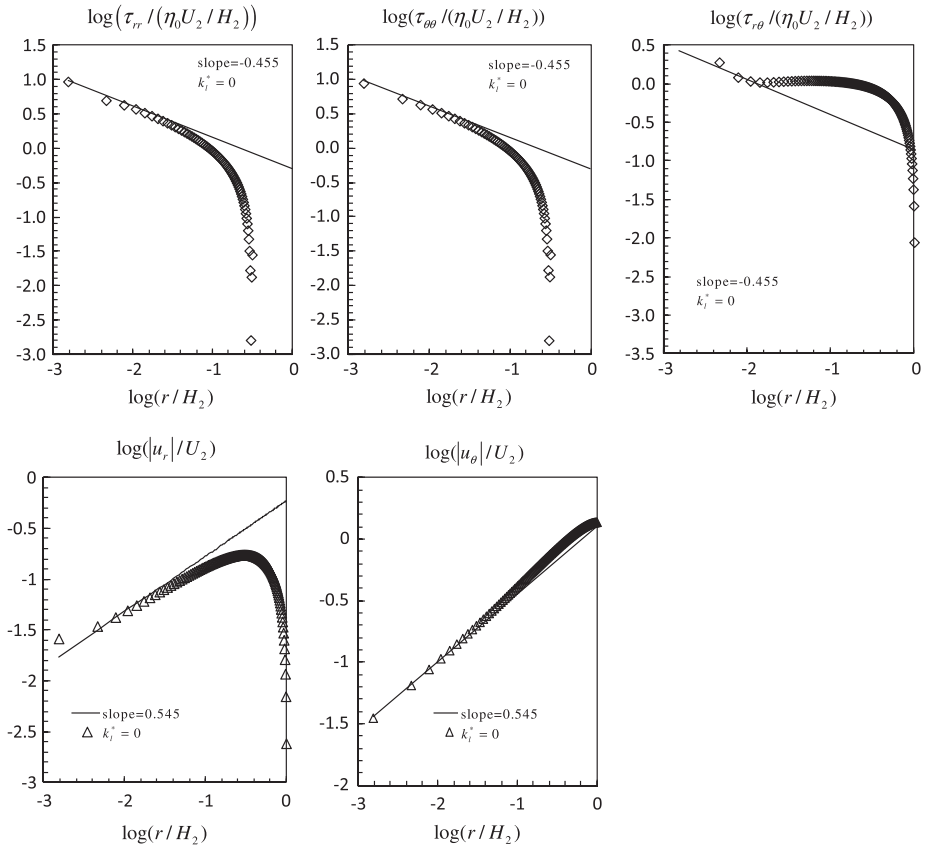

Fig. 6. Asymptotic behavior for the velocity and stress components near the reentrant corner of a 4:1 contraction, for a Newtonian fluid with $Re = 0.04$ and $k_l^* = 0$.

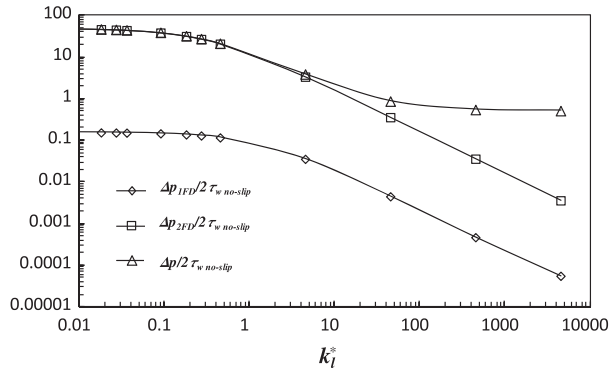

Fig. 8. Variation of the normalized real pressure drop, Δp, normalized Δp_{1FD} and normalized Δp_{2FD}, with the slip coefficient, for a Newtonian fluid at $Re = 0.04$.

where Δp represents the pressure drop between the entrance and the exit of the contraction (in regions where the flow is fully-developed), Δp_{1FD}, Δp_{2FD} denote the pressure drop for fully developed Poiseuille flow in the entry and exit channels (between the same points considered for Δp), with widths H_1 and H_2, respectively, and τ_w is the total wall shear stress (encompassing both solvent and polymer contributions) for fully-developed flow in the exit channel. A non-linear relationship between C and k_l^* is observed, as shown in Fig. 7(a). For small values of the slip coefficient we observe a slight increase in C followed by a sudden exponential increase. For $k_l^* = 0$ we obtained a value of $C = 0.3786$ ($C = 0.3741$ was obtained by Alves et al. [19] for $Re = 0$) while for $k_l^* = 4500$ we obtained $C = 6856$. These high values of the Couette correction are mainly an outcome of the small values of τ_w (a consequence of the increase of the slip coefficient) used in the normalization of Δp. Therefore we also plotted in Fig. 7(b) the modified Couette correction, C^*, normalized with the wall shear stress obtained from the no-slip case, $\tau_{w-no\ slip}$. In this case, for $k_l^* = 4500$ we obtained a value of $C^* = 0.5078$.

In order to understand why C^* increases with k_l^*, we plotted separately in Fig. 8 the three terms that make up C^*, i.e., the normalized real pressure drop $\left(\frac{\Delta p}{2\tau_{w-no\ slip}}\right)$ and the normalized Δp corresponding to fully-developed flow in the upstream $\left(\frac{\Delta p_{1FD}}{2\tau_{w-no\ slip}}\right)$ and downstream channels $\left(\frac{\Delta p_{2FD}}{2\tau_{w-no\ slip}}\right)$. It is clear that by increasing the slip coefficient these fully-developed pressure drops decrease significantly faster (and even tend to zero) than the reduction in the overall pressure drop, which includes the non-negligible entry pressure drop due to the strong extensional flow at the contraction.

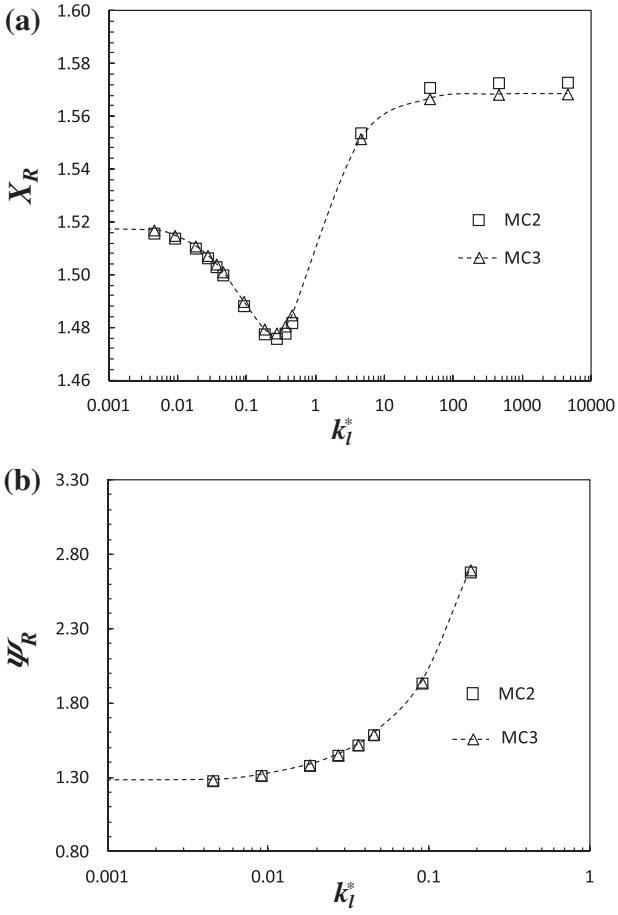

Fig. 9. Variation of the vortex dimension X_R (a) and vortex intensity Ψ_R (b) with the slip coefficient k_l^* for an sPTT fluid with $\varepsilon = 0.25$, $Re = 0.04$ and $De = 1$.

4.2. Viscoelastic fluid

4.2.1. Small elastic effects: De = 1

4.2.1.1. Vortex size, intensity and Couette correction. Table 2 presents the dimensionless vortex dimension X_R, vortex intensity Ψ_R and Couette correction C together with the relative error (relative difference between the results obtained with mesh MC3 and the results of mesh MC2) for the 4:1 contraction flow at $De = 1$.

Table 2
Vortex dimensions, intensity and Couette correction for an sPTT fluid flow with $\varepsilon = 0.25$, $Re = 0.04$, $De = 1$ (the values with $*$ are the results obtained for the lip vortex, that engulfs the corner vortex).

k_l^*	$X_{R\ MC3}$	Error (%)	$\Psi_{R\ MC3}$	Error (%)	C_{MC3}	Error (%)	C^*_{MC3}	Error (%)
0.0000	1.5180	0.077	1.2800	0.321	0.1021	0.375	0.1021	0.375
0.0045	1.5170	0.079	1.2830	0.323	0.1043	0.451	0.1038	0.452
0.0090	1.5149	0.067	1.3174	0.291	0.1065	0.323	0.1055	0.324
0.0180	1.5109	0.052	1.3851	0.261	0.1109	0.190	0.1087	0.191
0.0270	1.5073	0.058	1.4534	0.258	0.1154	0.172	0.1120	0.173
0.0360	1.5041	0.067	1.5218	0.178	0.1201	0.139	0.1153	0.139
0.0450	1.5011	0.077	1.5907	0.180	0.1249	0.133	0.1188	0.133
0.0900	1.4899	0.107	1.9412	0.298	0.1508	0.298	0.1363	0.298
0.1800	1.4794	0.120	2.6968	0.518	0.2124	0.496	0.1741	0.495
0.2700	1.4779	0.139	3.5460	0.610	0.2848	0.518	0.2124	0.517
0.3600	1.4806	0.180	4.7771*	0.987	0.3663	0.513	0.2494	0.512
0.4500	1.4848	0.196	6.2221*	0.945	0.4549	0.491	0.2838	0.489
4.5000	1.5516	0.143	25.536*	0.708	5.0802	0.495	0.5786	0.490
45.000	1.5667	0.271	31.633*	0.907	50.155	0.575	0.6095	0.569
450.00	1.5684	0.280	32.361*	0.939	500.31	0.543	0.6121	0.537
4500.0	1.5685	0.281	32.435*	0.943	5001.8	0.541	0.6123	0.325

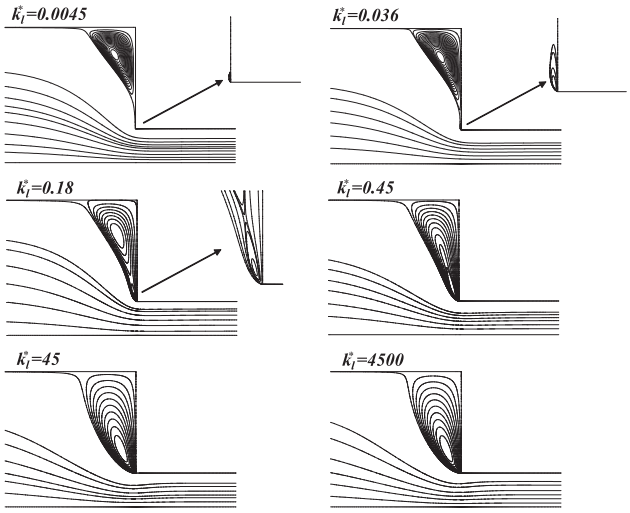

Fig. 10. Visualization of the corner and lip vortex growth with the dimensionless slip coefficient k_l^* for an sPTT fluid with $\varepsilon = 0.25$, $Re = 0.04$ and $De = 1$.

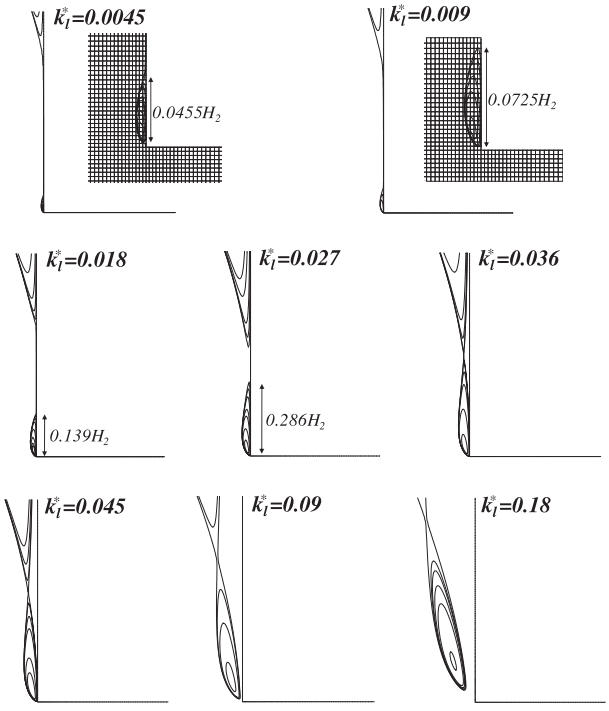

Fig. 11. Lip vortex growth for increasing values of the dimensionless slip coefficient k_l^* for an sPTT fluid with $\varepsilon = 0.25$, $Re = 0.04$ and $De = 1$.

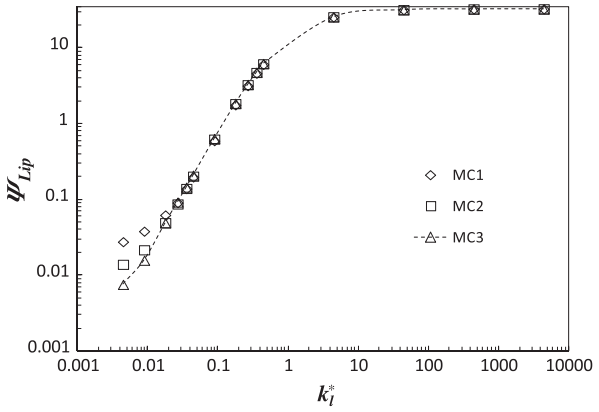

Fig. 12. Variation of the lip vortex intensity Ψ_{lip} with the dimensionless slip coefficient k_l^* for an sPTT fluid with $\varepsilon = 0.25$, $Re = 0.04$ and $De = 1$. Comparison of the results obtained in the three meshes used.

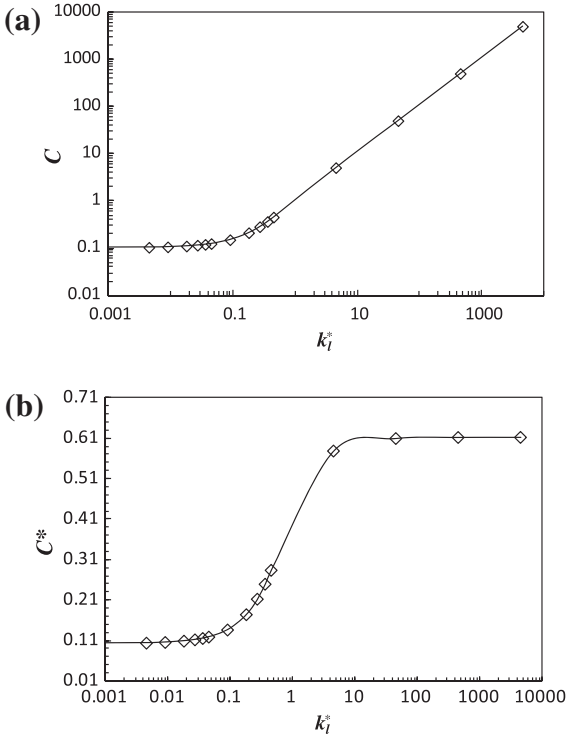

Fig. 13. Variation of the Couette correction with the dimensionless slip coefficient k_l^* for an sPTT fluid with $\varepsilon = 0.25$, $Re = 0.04$ and $De = 1$. (a) Couette correction (C) normalized with $2\tau_w$. (b) Couette correction (C^*) normalized with the wall shear stress from the no-slip case, $2\tau_{w-no\ slip}$. Results obtained with mesh MC3.

As shown in Fig. 9(a) the variation of X_R with k_l^* is nonmonotonic with a local minimum at $k_l^* \approx 0.2$ and subsequent increase in length, in strong contrast to the Newtonian fluid behavior. This is a consequence of the competition between viscous and elastic effects, both coupled with slip. At low values of k_l^*, and as for Newtonian fluids, the viscous effects predominate over the elastic effects and the reduction of the near wall shear rates associated with slip leads to a local reduction of dissipative effects and to a small decrease in X_R (notice that a region of separated flow is a fairly effective means of locally dissipating energy). However, as k_l^* increases the elastic effects also intensify, leading to the formation of a lip vortex which grows slowly for low values of k_l^* and more intensely as k_l^* increases, engulfing the corner vortex and increasing in size. The increase in X_R with k_l^* is asymptotic because the growth of the elastic recirculation is not dominated by the near wall forces, but by the normal stresses associated with the extensional flow in the central region of the contraction, so the vortex ceases to grow above $k_l^* \approx 100$ when the elongational type of flow ceases to change with k_l^*. Since the increase of slip reduces both the near-wall viscous shear stress and the elastic shear-induced normal stress, we show in this way that the corner vortex is essentially determined by viscous forces while the lip vortex and its growth are essentially determined by the extensional elastic stresses in the central region of the geometry.

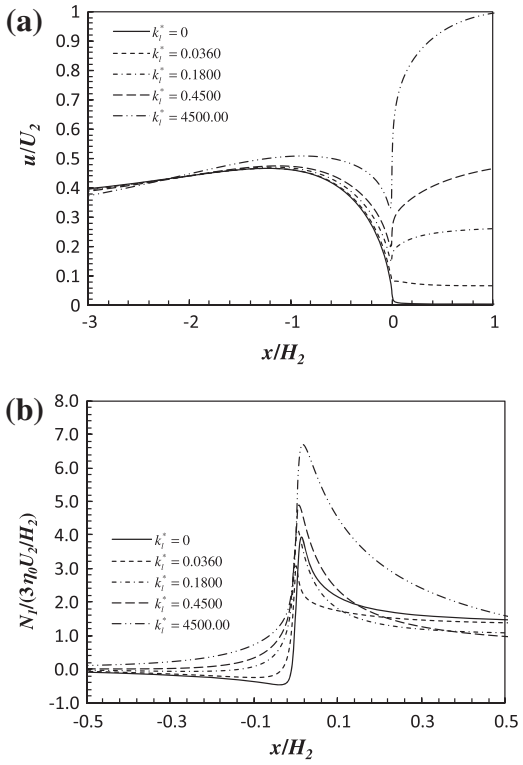

Fig. 14. Variation of the normalized velocity and first-normal stress difference fields along the line $y/H_2 = 0.9985$ as function of the slip coefficient k_l^* for an sPTT fluid with $\varepsilon = 0.25$ and $De = 1$: (a) u/U_2 and (b) $N_1/(3\eta_0 U_2/H_2)$. Results obtained with mesh MC3.

Regarding the corner vortex intensity, Fig. 9(b) shows that it increases with the increase of the slip coefficient and this increase is due at low values of k_l^* to the reduction of viscous losses within the vortex, already observed with Newtonian fluids, followed subsequently by the increasing effect of the enhanced elastically driven lip vortex. The specific values of Ψ_R have to be analyzed with care, especially when the corner and lip vortices co-exist given the distortion induced by each one on the other, with obvious consequences in terms of accuracy. For the three meshes used we find that for $k_l^* \simeq 0.03$ the two vortices begin to merge until a single and larger vortex is formed at $k_l^* \simeq 0.3$. Further increasing k_l^* leads to vortex growth and modifications in its curvature, as shown in the streamline plots of Fig. 10 (obtained using mesh MC3).

For the lip vortex dimension Y_{lip}, accurate results are much more difficult to obtain and require very refined meshes. This happens because the top part of the increasing lip vortex starts to rotate in the counterclockwise direction (as seen in Fig. 11) meaning that the results obtained for the Y_{lip} are deceived by that rotation.

Regarding the lip vortex intensity, Ψ_{lip}, Fig. 12 shows that it increases with the slip coefficient, but we could find the existence of a region of higher uncertainty at low k_l^*. This happens in the cases where the two vortices coexist and because their specific location is very sensitive to the mesh characteristics. Finally, the lip vortex becomes the main vortex above $k_l^* \simeq 0.3$ and high levels of vortex intensity are obtained. The existence of two vortices with one vortex engulfing and absorbing the other while increasing the elasticity was also found by Xue et al. [17] for an Oldroyd-B fluid employing the no-slip boundary condition. These features were also present in the high Deborah-number contraction flows investigated by Afonso et al. [22], in which the elastic lip vortex increases in size and eventually reaches the corner vortex region, and merges with it in a fairly complex dynamic process. This merging-growth regime occurs at $De \simeq 4.5$ for the Oldroyd-B model with no slip, corresponding to the minimum value of X_R [22].

The Couette correction was also calculated and we found a similar dependence on k_l^* as for the Newtonian fluid, increasing with the increase of the slip coefficient as shown in Fig. 13 and in Table 2.

4.2.1.2. Variation of velocity and stresses near the wall. In order to assess the effects of slip velocity on the distribution of velocity and normal stresses, the streamwise components of these variables were monitored near the downstream channel walls, along the horizontal line $y/H_2 = 0.9985$. For the velocity, Fig. 14(a) shows its smoothing with the increase of the slip velocity, except near the reentrant corner where a large gradient is usually found. For the dimensionless first-normal stress difference, $N_1 = \tau_{xx} - \tau_{yy}$ (normalized with $3\eta_0 U_2/H_2$) we observe, in Fig. 14(b), higher values near the singularity at higher k_l^* when compared to the no-slip boundary condition case.

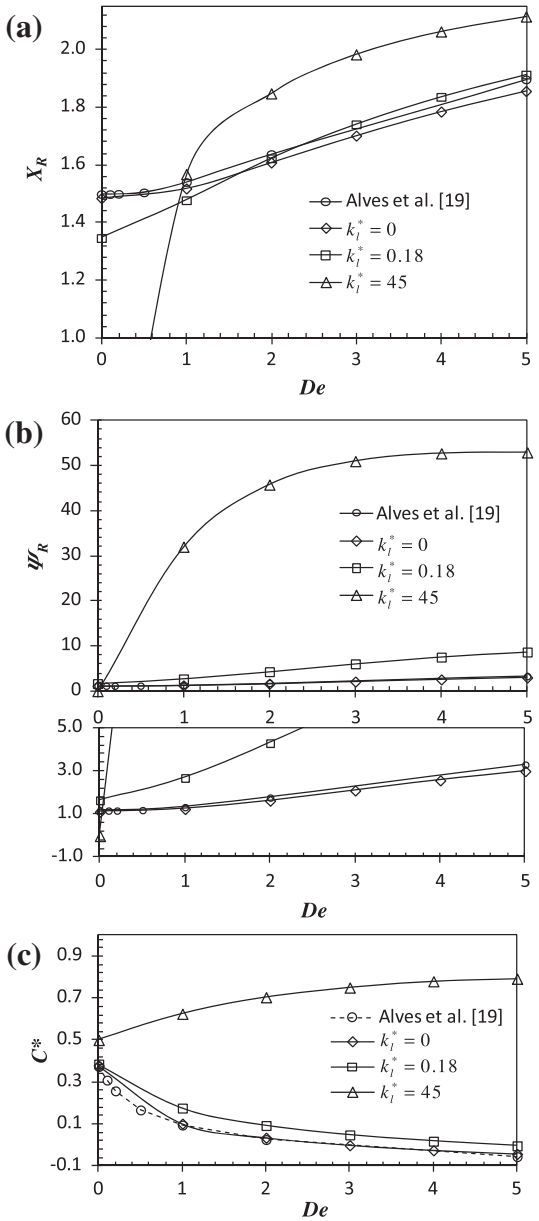

Fig. 15. Variation of the vortex dimension X_R (a), vortex intensity Ψ_R (b) and the Couette correction C^* (c) with De, for three different values of the slip coefficient: $k_l^* = 0$, $k_l^* = 0.18$ and $k_l^* = 45$ (the lines are only a guide to the eye and the reference Alves et al. [19] refers to no-slip case). Results obtained with mesh MC3.

4.2.2. Effect of elasticity

The 4:1 contraction flow was also simulated for more elastic flow conditions, including $De = 2, 3, 4$ and 5. For higher values of De convergence could not be achieved for high slip coefficients. This contrasts with the no-slip simulations of Alves et al. [19] with the sPTT fluid, which converged at least up to $De = 100$, using the same methodology. These results thus show that the slip velocity strongly influences the convergence properties of the sPTT fluid flow mainly due to the higher normal strain/stress gradients that occur near the reentrant corner. Notice also that the computations were performed on half of the domain, but it is known that the viscoelastic flow through a sudden contraction of some viscoelastic fluids, like the Oldroyd-B fluid, exhibits time dependency and is no longer symmetric above a critical De [22]. For $De = 0, 2, 3, 4$ and 5 the results qualitatively follow the same trends of the $De = 1$ case, as shown in Fig. 15. Fig. 15(a) plots the vortex size whereas Fig. 15(b) shows that the vortex intensity Ψ_R and the vortex size X_R both increase with the Deborah number for several constant values of slip coefficient ($k_l^* = 0; 0.18; 45$) and also increase with slip coefficient at constant De. As an example, for $De = 5$ $\Psi_R \approx 3$ for the no-slip case, and increases up to $\Psi_R \approx 50$ for $k_l^* = 45$ (see Fig. 15(b)). For the modified Couette correction C^* we see that the presence of wall slip velocity leads to an extra pressure loss ($C^* > 0$).

5. Conclusions

Numerical simulations were performed for the flow of Newtonian and non-Newtonian fluids past an abrupt 4:1 planar contraction in the presence of wall slip. To model the non-Newtonian fluid the sPTT constitutive equation was used and slip on all walls was described by the linear Navier slip law. Slip was found to have a dramatic impact upon the dynamics of separated flow upstream of the contraction, especially for viscoelastic fluids.

For the Newtonian fluid the vortex decreases in size until it eventually disappears with increasing slip velocity, even though for weak values of slip a slight increase in vortex intensity was observed. Although it seems unlikely for a Newtonian fluid to present these high levels of slip velocity, the results are helpful for the interpretation of the slip effects.

For non-Newtonian fluids the corner vortex tends to decrease with slip, but only for low values of the slip coefficient, along with the formation of a lip vortex. As slip increases the lip vortex grows, engulfs and absorbs the corner vortex, promoting an increase in size and curvature modification of the flow recirculation boundary, very much as previously observed with Oldroyd-B fluids without wall slip. It was also found that the vortex dimensions increase with De, thus slip enhances significantly the effect of elasticity observed in the no-slip cases. For $De > 5$ it was not possible to achieve convergence with wall slip, mainly due to the high stress gradients appearing near the re-entrant corner. Considering that in the absence of slip, and for the same constitutive model, Alves et al. [19] were able to obtain converged solutions up to De of order 100 it is clear that the high Deborah-number problem is enhanced by the presence of wall slip. These results are useful to interpret and model fluids subjected to slip boundary conditions such as some polymer systems used in polymer processing industries.

Acknowledgements

The authors gratefully acknowledge funding by COMPETE, FEDER and Fundação para a Ciência e a Tecnologia (FCT) through projects PEst-C/CTM/LA0025/2013 (Strategic Project - LA 25 – 2013-2014, PTDC/EME-MFE/113988/2009 and PTDC/EME-MFE/114322/2009. AMA would also like to thank FCT for the financial support through the scholarship SFRH/BPD/75436/2010.

References

[1] S. Kim, J.M. Dealy, Gross melt fracture of polyethylene. I: A criterion based on tensile stress, Polym. Eng. Sci. 42 (2002) 482–494.
[2] M. Miller, A. Luciani, A. Sarioglu, J.E. Mason, Flow through a convergence. Part 1: Critical conditions for unstable flow, Polym. Eng. Sci. 42 (2002) 611–633.
[3] R.G. Owens, T.N. Phillips, Computational Rheology, Imperial College Press, London, 2002.
[4] D.V. Boger, K. Walters, Rheological Phenomena in Focus, Elsevier, New York, 1993.
[5] M.A. Alves, R.J. Poole, Divergent flows in contractions, J. Non-Newton. Fluid Mech. 144 (2007) 140–148.
[6] R.J. Poole, M.P. Escudier, A. Afonso, F.T. Pinho, Laminar flow of a viscoelastic shear-thinning liquid over a backward-facing step preceded by a gradual contraction, Phys. Fluids 19 (2007) 093101:1–17.
[7] A. Afonso, F.T. Pinho, Numerical investigation of the velocity overshoots in the flow of viscoelastic fluids inside a smooth contraction, J. Non-Newton. Fluid Mech. 139 (2006) 1–20.
[8] M.A. Alves, F.T. Pinho, P.J. Oliveira, Visualizations of Boger fluid flows in a 4:1 square–square contraction, AIChE J. 51 (2005) 2908–2922.
[9] M.A. Alves, F.T. Pinho, P.J. Oliveira, Viscoelastic flow in a 3D square/square contraction: visualizations and simulations, J. Rheol. 52 (2008) 1347–1368.
[10] G.H. McKinley, W.P. Raiford, R.A. Brown, R.C. Armstrong, Nonlinear dynamics of viscoelastic flow in axisymmetric abrupt contractions, J. Fluid Mech. 223 (1991) 411–456.
[11] E.J. Hinch, The flow of an Oldroyd fluid around a sharp corner, J. Non-Newton. Fluid Mech. 50 (1993) 161–171.
[12] M. Renardy, A matched solution for corner flow of the upper convected Maxwell fluid, J. Non-Newton. Fluid Mech. 58 (1995) 83–89.
[13] J.D. Evans, D.N. Sibley, Re-entrant corner flows of PTT fluids in the Cartesian stress basis, J. Non-Newton. Fluid Mech. 153 (2008) 12–24.
[14] J.D. Evans, D.N. Sibley, Re-entrant corner flows for PTT fluids in the natural stress basis, J. Non-Newton. Fluid Mech. 157 (2009) 79–91.
[15] R. Keunings, Simulation of viscoelastic fluid flow, Fundam. Comput. Model. Polym. Process. (1989).
[16] J.Y. Yoo, Y. Na, A numerical study of the planar contraction flow of viscoelastic fluids using the SIMPLER algorithm, J. Non-Newton. Fluid Mech. 39 (1991) 89–106.
[17] S.C. Xue, N. Phan-Thien, R.I. Tanner, Three dimensional numerical simulations of viscoelastic flows through planar contractions, J. Non-Newton. Fluid Mech. 74 (1998) 195–245.
[18] M. Aboubacar, M.F. Webster, A cell-vertex finite volume/element method on triangles for abrupt contraction viscoelastic flows, J. Non-Newton. Fluid Mech. 98 (2001) 83–106.
[19] M.A. Alves, P.J. Oliveira, F.T. Pinho, Benchmark solutions for the flow of Oldroyd-B and PTT fluids in planar contractions, J. Non-Newton. Fluid Mech. 110 (2003) 45–75.
[20] M.A. Alves, P.J. Oliveira, F.T. Pinho, On the effect of contraction ratio in viscoelastic flow through abrupt contractions, J. Non-Newton. Fluid Mech. 122 (2004) 117–130.
[21] Y. Kwon, J. Han, Convergence limit in numerical modeling of steady contraction viscoelastic flow and time-dependent behavior near the limit, Korea–Aust. Rheol. 22 (2010) 237–245.
[22] A.M. Afonso, P.J. Oliveira, F.T. Pinho, M.A. Alves, Dynamics of high-Deborah-number entry flows. A numerical study, J. Fluid Mech. 677 (2011) 277–304.
[23] A. Sunarso, T. Yamamoto, N. Mori, Numerical simulation of polymeric flow in contraction channels: wall slip and channel size dependent effects, in: FLOW DYNAMICS: The Second International Conference on Flow Dynamics. AIP Conference Proceedings, vol. 832, 2006, pp. 341–344.
[24] A. Sunarso, T. Yamamoto, N. Mori, Numerical analysis of wall slip effects on flow of Newtonian and non-Newtonian fluids in macro and micro contraction channels, J. Fluids Eng. 129 (2007) 23–31.
[25] K. Yasuda, Y. Sugiura, Entry flows of polymer solutions through a planar contraction in a microchannel, J. Fluid Sci. Technol. 3 (2008) 987–998.
[26] Y.M. Joshi, M.M. Denn, Planar contraction flow with a slip boundary condition, J. Non-Newton. Fluid Mech. 114 (2003) 185–195.
[27] S. Nigen, K. Walters, Viscoelastic contraction flow: comparison of axisymmetric and planar configurations, J. Non-Newton. Fluid Mech. 102 (2002) 343–359.
[28] S.G. Hatzikiriakos, J.M. Dealy, Wall slip of molten high density polyethylene. I. Sliding plate rheometer studies, J. Rheol. 35 (1991) 497–523.
[29] S.G. Hatzikiriakos, J.M. Dealy, Wall slip of molten high density polyethylene. II. Capillary rheometer studies, J. Rheol. 36 (1992) 703–741.
[30] H. Münstedt, M. Schmidt, E. Wassner, Stick and slip phenomena during extrusion of polyethylene melts as investigated by laser-Doppler velocimetry, J. Rheol. 44 (2000) 413–427.
[31] L.L. Ferrás, J.M. Nóbrega, F.T. Pinho, Implementation of slip boundary conditions in the finite volume method: new techniques, Int. J. Numer. Meth. Fluids 72 (2013) 724–747.
[32] N. Phan-Thien, R.I. Tanner, A new constitutive equation derived from network theory, J. Non-Newton. Fluid Mech. 2 (1977) 353–365.
[33] C.L.M.H. Navier, Sur les lois du mouvement des fluids, Mem. Acad. Roy. Sci. Inst. Fr. 6 (1827) 389–440.
[34] J.P. Van Doormaal, G.D. Raithby, Enhancement of the SIMPLE method for predicting incompressible fluid flows, Numer. Heat Transfer 7 (1984) 147–163.

[35] P.J. Oliveira, F.T. Pinho, G.A. Pinto, Numerical simulation of non-linear elastic flows with a general collocated finite-volume method, J. Non-Newton. Fluid Mech. 79 (1998) 1–43.
[36] H.K. Moffatt, Viscous and resistive eddies near a sharp corner, J. Fluid Mech. 18 (1964) 1–18.
[37] W.R. Dean, P.E. Montagnon, On the steady motion of viscous liquid in a corner, Proc. Cambridge Philos. Soc. 45 (1949) 389–394.
[38] P.J. Coates, R.C. Armstrong, R.A. Brown, Calculation of steady-state viscoelastic flow through axisymmetric contractions with the EEME formulation, J. Non-Newton. Fluid Mech. 42 (1992) 141–188.